ADVANCES IN ATMOSPHERIC SCIENCES, VOL. 35, OCTOBER 2018, 1243–1253

• **Original Paper** •

A High-Resolution Modeling Study of the 19 June 2002 Convective Initiation Case during IHOP_2002: Localized Forcing by Horizontal Convective Rolls

Qi-Wei WANG[1] and Ming XUE*[1,2]

[1] *Key Laboratory of Mesoscale Severe Weather and School of Atmospheric Sciences Nanjing University, Nanjing* 210023*, China*
[2] *Center for Analysis and Prediction of Storms and School of Meteorology University of Oklahoma, Norman Oklahoma* 73072*, USA*

(Received 8 September 2017; revised 26 February 2018; accepted 21 March 2018)

ABSTRACT

The initiation processes of one of the initial convective cells near and on the east side of a dryline on 19 June 2002 during the IHOP_2002 field experiment in the central United States is analyzed in detail based on a high-resolution numerical simulation. Prominent horizontal convective rolls and associated near-surface moisture convergence bands [called roll convergence bands (RCBs) here] develop within the convective boundary layer (CBL) due to surface heating, in the hours leading to convective initiation (CI). The RCBs east of the dryline are advected toward the primary dryline convergence boundary (PDCB) by the southerly moist flow as the CBL deepens with time. Backward trajectories of air parcels forming the initial precipitating updraft of the convective cell are found to primarily originate at about 1–1.5 km above ground, within the upper portion of the shallower CBL earlier on. The representative air parcel is found to follow and stay on top of a surface RCB as the RCB moves toward the PDCB, but the RCB forcing alone is not enough to initiate convection. As this RCB gets close to the PDCB, it moves into a zone of mesoscale convergence and a deeper CBL that exhibits an upward moisture bulge associated with the PDCB. The combined upward forcing of the RCB and the mesoscale PDCB convergence quickly lifts the representative air parcel above its level of free convection to initiate convection. A conceptual model summarizing the CI processes is proposed.

Key words: convective initiation, dryline, localized forcing, horizontal convective rolls

Citation: Wang, Q.-W., and M. Xue, 2018: A high-resolution modeling study of the 19 June 2002 convective initiation case during IHOP_2002: Localized forcing by horizontal convective rolls. *Adv. Atmos. Sci.*, **35**(10), 1243–1253, https://doi.org/10.1007/s00376-018-7218-3.

1. Introduction

The forecasting of severe convective storms and quantitative precipitation remains a major challenge for both numerical weather prediction models and for operational weather forecasters, largely due to the big uncertainty in the convective initiation (CI) forecast (e.g., Fritsch and Carbone, 2004; Richard et al., 2007). The CI is often associated with complex interactions of multi-scale forcings, including the large-scale upper-tropospheric forcing, low-level mesoscale convergence forcing at frontal zones and other boundaries, and local-scale circulations associated with boundary layer (BL) processes. The CI processes can vary from case to case and region to region, because the forcings involved are often associated with distinct weather systems and geographical conditions. Several field campaigns have been carried out in recent years to address the CI problem, including IHOP_2002 in the southern Great Plains of the United States (Weckwerth and Parsons, 2006; Weckwerth et al., 2004), the Convective Storm Initiation Project in the southern United Kingdom (Browning et al., 2007), and the Convective and Orographically Induced Precipitation Study in the low-mountain region of southwestern Germany/eastern France (Wulfmeyer et al., 2008).

The CI in the IHOP_2002 region in the spring–summer season is often forced by mesoscale circulations associated with dryline and/or frontal or thunderstorm outflow boundaries (e.g., Bluestein and Parker, 1993; Hane et al., 1993; Ziegler and Hane, 1993; Ziegler et al., 1995; Shaw et al., 1997; Ziegler and Rasmussen, 1998; Atkins et al., 1998; Hane et al., 2002; Peckham et al., 2004; Trier et al., 2015). The pre-convective environment for CI is generally characterized by high convective instability with a strong capping inversion. Although the mesoscale environment and forcing along a quasi-two-dimensional front or dryline are often similar, convection seldom uniformly initiates along the front or dryline. Instead, the CI often starts at specific locations, but such locations and the exact timing of CI are very difficult to predict accurately because they are often determined by fine-

* Corresponding author: Ming XUE
Email: mxue@ou.edu

scale local forcings and their interactions with the mesoscale environment. Horizontal convective rolls (HCRs) can induce such fine-scale local forcings when they interact with the dryline mainly from the west side (e.g., Atkins et al., 1998) or the primary dryline convergence boundary (PDCB) from the dryline transition zone (e.g., Xue and Martin, 2006a, b).

HCRs on the east side of a dryline can also interact with a dryline and trigger convection. Peckham et al. (2004) discussed the role of HCRs east of a dryline in the formation of deep cumulus clouds in an idealized simulation. HCRs and open convective cells (OCCs) east of the dryline were found to impact the convective cloud locations by modulating the low-level moisture and upslope easterly flow. Shallow convective clouds initially form along and west of the dryline over the OCC and HCR updrafts, as well as OCC-dryline and HCR-dryline intersection points. The OCCs and HCRs east of the dryline tend to intersect the dryline and enhance the shallow convective clouds above, instead of triggering convection alone through interacting with the dryline. In the real world, convection is often found initiating along the dryline due to forcing on the east side of the dryline and richer moisture supply there, but the CI associated with HCRs is still not well understood.

Following a similar modeling approach to Xue and Martin (2006a, b) and Liu and Xue (2008), and using grid spacings of up to 1 km and initial conditions that assimilate all available high-resolution observations, including special datasets collected by IHOP_2002, Wang and Xue (2012) obtained a rather successful simulation of the 19 June 2002 CI case from IHOP_2002 (Wilson and Roberts, 2006). In Wang and Xue (2012), circulations associated with BL HCRs and OCCs are abundant, and they are superimposed on top of the mesoscale circulations and appear to provide additional localized lifting that determines the locations of first cell initiations. Wang and Xue (2012) did not, however, examine the detailed temporal evolution of the fine-scale structures associated with the HCRs or OCCs or their specific role in initiating the first convective cells. Their study was limited to examining how mesoscale features, including low-level mesoscale convergence and moisture bands, provide generally favorable conditions for CI. The exact processes that determine the preferred locations for the initiation of first cells need to be further investigated, especially for the second CI group in Wang and Xue (2012), which is focused on in IHOP_2002. This paper analyzes the exact processes associated with the first cell of the second CI group in Wang and Xue (2012) by performing detailed trajectory-based analyses and other diagnostics. Such an approach was not taken by similar earlier studies, including Xue and Martin (2006a, b) and Liu and Xue (2008), who studied two other CI cases from IHOP_2002.

The rest of this paper is organized as follows: In section 2, the development and evolution of the BL HCRs and their interactions with the dryline within the 1-km numerical simulation are analyzed in detail. The mechanisms that trigger the first convective cell are discussed in section 3. A summary is given in section 4, including a conceptual model of the CI proposed.

2. Development and evolution of HCRs preceding CI

At noon local standard time, or 1800 UTC 19 June 2002, a main cold front stretched from a low center located at eastern South Dakota, through far northwestern Kansas, into eastern Colorado and then toward the south-central Colorado–New Mexico border. At the same time, a dryline extended from the cold front at northwestern Kansas through the Kansas–Colorado border, into far southeastern Colorado and then into eastern New Mexico (Fig. 1). On this day, the CIs focused in IHOP_2002 are at the dryline close to the cold-front-dryline "triple point" in northwestern Kansas (box region in Fig. 1); and data from airborne Doppler radar, aircraft dropsondes, and other mobile research platforms were available (Murphey et al., 2006), and were used to verify the numerical simulation analyzed in Wang and Xue (2012). The exact processes of the first CI in this region are further analyzed in this paper.

As in Wang and Xue (2012), the model outputs that we focus our attention on for detailed diagnostic analysis come from a control simulation at 1-km grid spacing using the Advanced Regional Prediction System (ARPS) (Xue et al., 2000, 2001). The control simulation started from an interpolated initial condition at 1800 UTC 19 June 2002, obtained from the National Centers for Environmental Prediction (NCEP) Eta Model analyses with assimilation of surface and other observations on a 3-km grid using the three-dimensional variational (3DVAR) data analysis scheme (Gao et al., 2004). The 1-km simulation was nested inside the 3-km

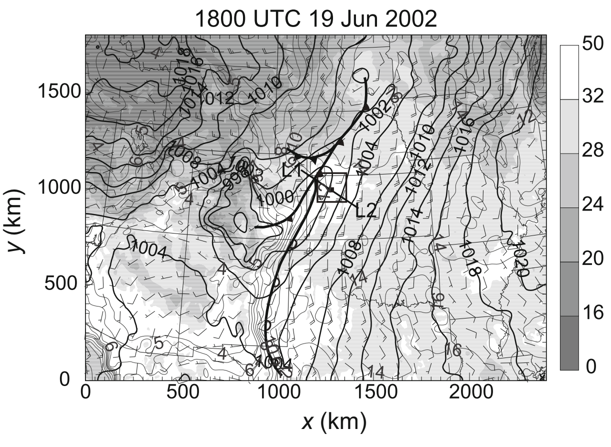

Fig. 1. The mean sea level pressure (thick black contours; units: hPa), surface temperature (shaded; units: °C), water vapor mixing ratio (thin black contours; units: g kg^{-1}), and the wind field (full barb represents 5 m s^{-1} and half barb 2.5 m s^{-1}) at 1800 UTC 19 June 2002, plotted from the Eta 40-km analysis. The cold front and dryline are marked by standard symbols [reproduced from Wang and Xue (2012)]. The small filled square marks the location of the first cell in the CI region. Line L1–L2 shows the positon of the vertical cross sections in Fig. 2. The square box corresponds to the CI region focused in Wang and Xue (2012), and is enlarged in Fig. 3.

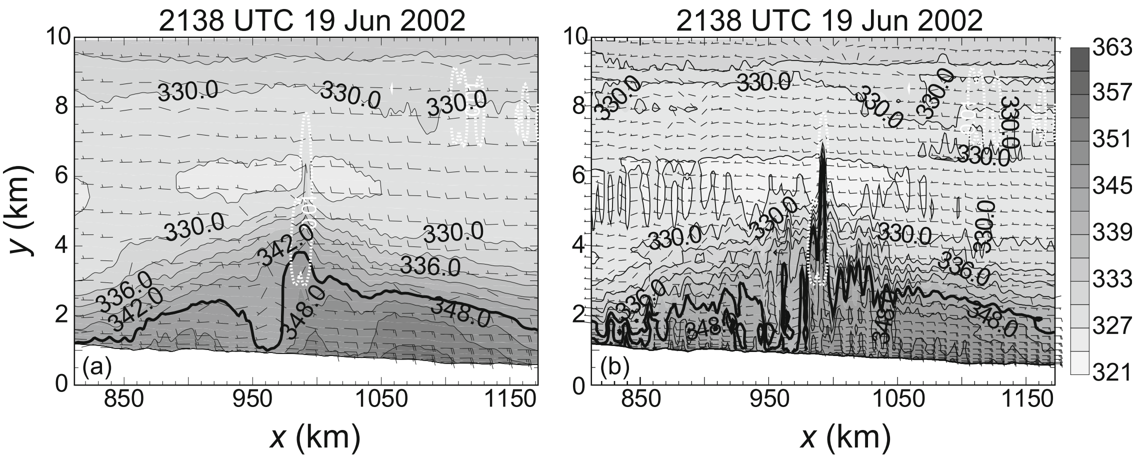

Fig. 2. Vertical cross section plotted along line L1–L2 (Fig. 1) at the CI time. Plots are equivalent potential temperature (θ_e; shaded with contours; units: K) and horizontal vector winds projected onto the cross section (wind barbs). In (a), two-dimensional smoothing was applied to the fields before plotting [reproduced from Wang and Xue (2012)]. The plots of (a) without smoothing are shown in (b). The 0.01 g kg^{-1} total condensed water/ice is shown in all the plots to outline the clouds (white dotted contours). The bold contour of θ_e at 346 K denotes the extent of the CBL.

grid, and has 1003×1003 horizontal grid points and 53 vertical levels defined on a generalized terrain-following coordinate, with the grid spacing increasing from about 20 m near the ground to about 800 m near the model top at about 20 km height [see Fig. 4 of Wang and Xue (2012)].

For the CI, it was further shown via vertical cross sections that the uplifting associated with low-level convergence at the dryline was instrumental in elevating the top of the convective boundary layer (CBL), resulting in a deep well-mixed BL whose top eventually reaches the level of free convection at certain locations (Fig. 2a). This deepened BL, being fed by air from the moist side of the dryline, is rich in moisture. It was further noticed that small-scale structures exist in the equivalent potential temperature spaced at about 10 km apart; these small-scale structures are much more evident in the non-smoothed version of their Fig. 2a, presented here as Fig. 2b, e.g., the 346-K contour that roughly denotes the extent of the CBL. It was suggested that these small-scale structures, superimposed on top of the mesoscale upwelling, provide additional forcing for initiating localized convection. These structures are believed to be linked to HCRs and BL OCCs; their general role is believed to be similar to those discussed in Xue and Martin (2006b), but the specific details can be quite different. These details are examined in this and subsequent sections.

The BL convective eddy and roll activities at the CI time can be clearly seen from the plots of low-level moisture convergence fields. Figure 3 shows these fields at about 30 m above ground level (AGL) at 2138 19 June 2002, the time of CI in the simulation. In Fig. 3, moisture convergence bands associated with HCRs [called roll convergence bands (RCBs) here] are mostly found east of the dryline and between the dryline and cold front. The bands west of the cold front show more of the OCC structures. The small RCBs to the east side of the dryline are well organized, and they are spaced about 10 km apart and are roughly parallel to the PDCB. The

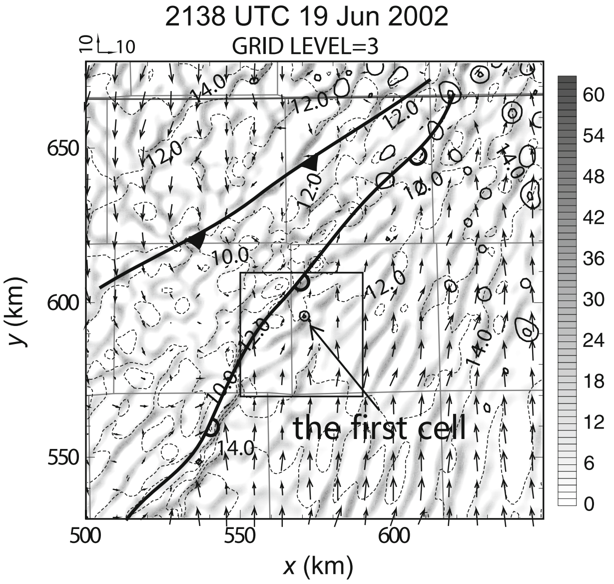

Fig. 3. Model-predicted near-surface (about 30 m AGL) moisture convergence field (gray shading; values amplified by a factor of 1000; only positive values shown), horizontal wind vectors (vector key shown in the plot; units: m s^{-1}), water vapor q_v field (thin-dashed contours), and composite reflectivity (full thick contours) for the CI at 2138 UTC 19 June 2002. The time corresponds to when 10–20 dBZ echoes of the cell (denoted with arrows) were first predicted (roughly when the the cell first initiates). The cold front and dryline are denoted with standard symbols. An enlarged view of the boxed region is shown in Fig. 5.

parallel RCBs tend to reorganize in the southerly moist flow before they merge into the convergence bands at the PDCB. It seems the reorganization of the RCBs induces a low-level convergence maximum, which provides local forcing to initiate the first convective cell. The detailed processed are discussed in section 3.

3. Initiation of the convective cell

3.1. *Representative parcel feeding the cell*

To facilitate more detailed analyses of the initiation of the cell, the air parcels at different levels within the updraft column possibly supporting the initiation of the cell are tracked forward and backward starting from the initial cloud stage at 2119 UTC and the initial cell stage at 2138 UTC of the CI (Fig. 4). The trajectories are calculated using the output of the 1-km numerical simulation at an interval of 1 min. The trajectories starting from the initial cloud stage cannot sample well the initiation of the cell (Figs. 4a and c). The forward trajectories from the initial cloud are disperse and the wavy patterns of the trajectories indicate evident entrainment occurred during the transition of the initial cloud to the initial cell; some parcels were even brought downward from the cloud level (Fig. 4c).

Instead, the initiation of the cell can be tracked well by the air parcels near the center of the updraft core below the initial cell at 4 km AGL (blue trajectories in Figs. 4b and d). The air parcels come primarily from an elevated layer of about 1–1.5 km AGL and run into the cell in a coincident manner (Fig. 4d). The trajectory of the initial parcel at the

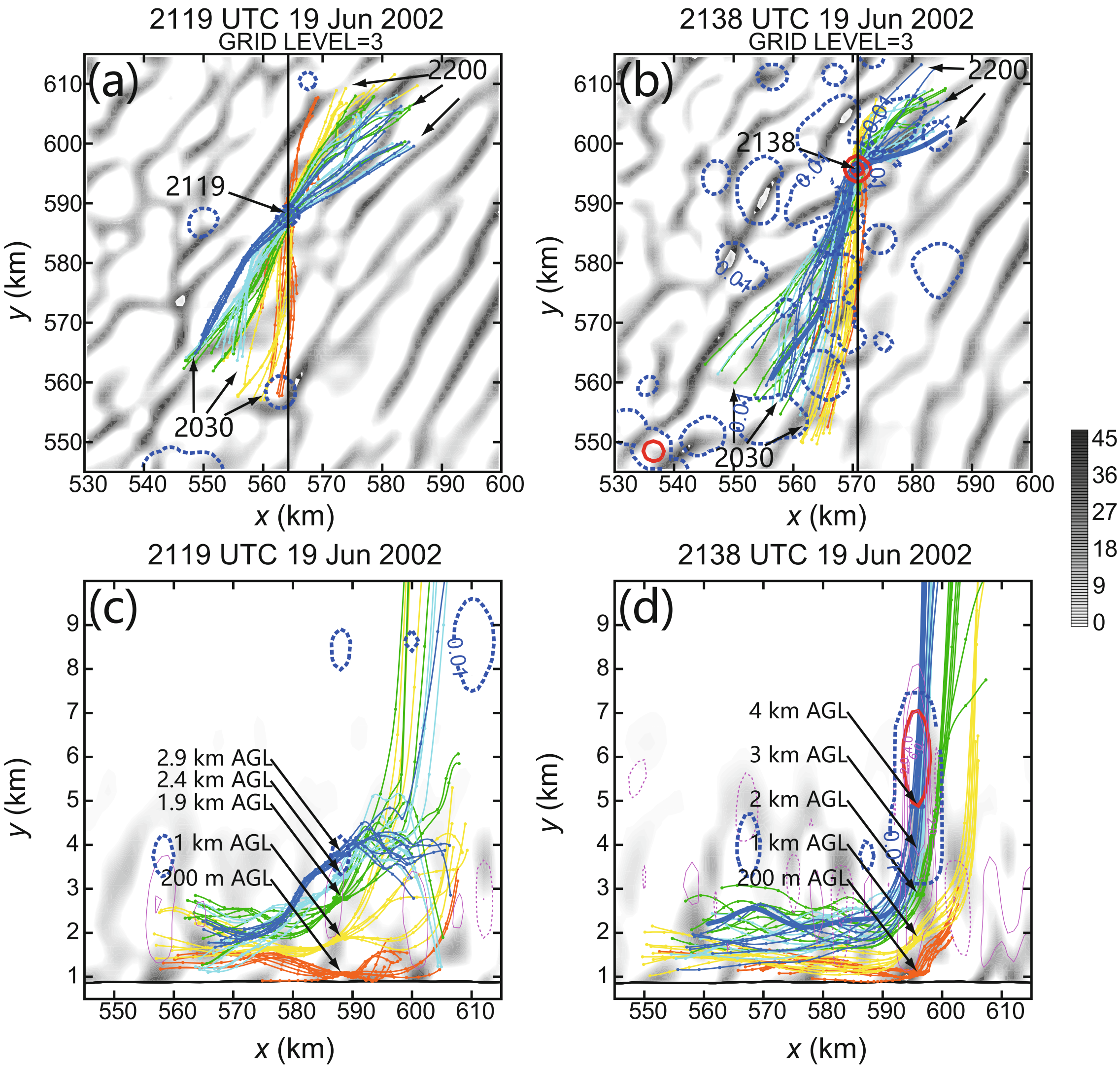

Fig. 4. Forward and backward trajectory analyses for air parcels at different levels within the updraft column possibly supporting the initiation of the cell at (a, c) 2119 (initial cloud stage) and (b, d) 2138 (initial cell stage) UTC 19 June 2002. The vertical cross sections (c) and (d) run through the lines in the horizontal panels (a) and (b) respectively. The end times of the forward and backward trajectory analyses are 2030 and 2200 UTC 19 June 2002, as denoted in (a) and (b). The trajectory groups with different colors start from the initial parcels at different levels, which are denoted in (c) and (d). At each level, nine parcels are sampled, with one at the center of the updraft column and eight uniformly located on a circle with radius 1 km from the center. The clouds are outlined as 0.01 g kg^{-1} total condensed water/ice (dotted blue contours) and the initial cells are shown as red bold contours of 10 and 20 dBZ echoes. The thin pink lines in (c) and (d) show the vertical velocity field (at 1 m s^{-1} intervals without zero contour, negative dashed). The gray shading shows the moisture convergence field (values amplified by a factor of 1000, and only positive values shown).

center of the updraft column is selected as the representative trajectory (thick blue trajectory in Fig. 4d) and is shown in the following plots, in the form of projection to the horizontal or vertical plan. The air parcels at 1, 2 and 3 km AGL reach their level of free convection slightly later than that at 4 km AGL, partially supporting the development of the cell or triggering new convection (Fig. 4d). The air parcels near the surface, meanwhile, e.g., at 200 m AGL, are associated with HCRs and only evolve roughly under the level of about 1 km AGL (Fig. 4d).

3.2. *Upward forcing of locally enhanced RCB*

We further show zoomed-in plots in Fig. 5, for the box region in Fig. 3, at times spanning the initiation. In addition to the fields plotted in Fig. 3, vertical vorticity is added to investigate the role of mesocyclones in CI. The contributions of HCR and mesocyclones to CI are analyzed by examining their effects on the representative air parcel feeding the initially triggered cell. The times of the parcel on the trajectory are labeled. Corresponding to Fig. 5, "curved" vertical cross sections plotted along the trajectories are shown in Fig. 6. These vertical cross sections are like curved "curtains" passing through the parcel trajectories, at the instances corresponding to the air parcel location indicated by the large dot on the trajectory (e.g., Fig. 6). The horizontal axis is the horizontal distance along the trajectories and the origin is at the southern boundary of the corresponding horizontal cross section plots (e.g., Fig. 5).

The location of the PDCB is indicated by the long-dashed straight lines in Fig. 5. Short-dashed lines labeled "Rn", where "n" is an integer number, denote bands of enhanced moist convergence due to HCRs or RCBs. Labels "Dn" and "Vn" in Fig. 5 indicate divergence centers and mesocyclones, respectively, which appear to play important roles in shaping or reorganizing the RCBs and modifying the enhanced updrafts that trigger convection.

The cell is initiated ahead of the dryline in a region where the near-surface HCRs show clear quasi-two-dimensional structures (Fig. 5). The PDCB in Fig. 5 is shown as a long-dashed line in a region of about 11–12 g kg^{-1} water vapor mixing ratio with a position consistent with the one more clearly defined in Fig. 3. The cell is initiated on the moist side of the PDCB where the RCBs interact with each other and with the PDCB. At 2100 UTC (Fig. 5a), RCB R0 is located at the PDCB and induces a band of strong moisture convergence. RCBs R1, R2 and R3 are found southeast of R0 and are roughly parallel to the PDCB, and are spaced roughly 10 km from each other. Between the RCBs are divergence zones that develop more three-dimensional structures as the RCBs develop some wavy patterns in response to the formation of mesocyclones (labelled V1–V3 in the figures) along the bands. As discussed in Xue and Martin (2006a), the divergence flows between the RCBs show asymmetric patterns, with the northeastward wind components being stronger in this case due to downward transport of southwesterly momentum from the above. The mesocyclones are about 90° out of phase with the nearby maximal moist convergence, and the vertical vorticity fields near the surface are also about 90° out of phase with the quasi-two-dimensional rolls. The generation of the vertical vorticity is associated with the titling of the (northwest pointing) horizontal vorticity associated with the sheared southwesterly prevailing wind by the roll circulation, which causes the establishment of positive vertical vorticity at the right (looking downstream of the prevailing wind) of the surface convergence band (or roll updraft).

Overall, there is a tendency for the RCBs on both sides (more pronounced for those on the east side) of the PDCB to be "advected" toward the PDCB, and some of the bands are merged into the PDCB. This is clearly shown for RCB R0 in Fig. 5. At 2100 UTC (Fig. 5a), R0 is partially merged into PDCB, while R1 is still one full "wavelength" away from the PDCB. At 2115 UTC (Fig. 5b), R1 is more or less a straight line, but with mesocyclone V1 gaining strength at its middle portion. The intensification of V1 causes breakup of R1 into two segments by 2127 UTC (Fig. 5c), with its southern segment quickly merging into the PDCB while the northern segment moves closer to the PDCB. Associated with the breakup of R1 and under the influence of the V1 circulation, divergence center D1 is split into D1 and D1' (Fig. 5c), with D1' being located on the east side of the eventually reconnected R1 and D1 remaining on its west side (Fig. 5e). The V1 circulation and D1' appear to enhance the convergence on RCB R2 at the location of an air parcel that ends up in the initiation of the cell (Figs. 5b–d). The breakup of an RCB by a mesocyclone and the associated splitting of a divergence center on the west side of the RCB and south of the mesocyclone also occurs with R2, where D2 is split into D2 and D2' by V3. In addition to V1 and D1', the approaching R3 and V2 on R2 may also have played a role in locally enhancing the low-level convergence along R2 at the parcel location. At the later times, R3 becomes rather close to R2 (Figs. 5e and f), and may eventually merge R2.

The parcel tracing the initiation of the cell is found to continuously follow the near-surface RCB R2 (Fig. 5). At 2100 UTC, the parcel is found on R2 at $y \approx 575$ km (Fig. 5a); over the next two time periods the parcel moves more or less northward while R2 moves northwestward. Despite the movement of R2, the parcel happens to stay above R2 all the time (Figs. 5b–d). As the local low-level convergence along R2 becomes strong enough and the parcel moves above, the convection quickly initiates (Figs. 5e and f).

The contribution of the locally enhanced near-surface convergence forcing along R2 to the CI is shown in the vertical cross sections plotted along the trajectory of the parcel in Fig. 6. The parcel originates from about 1–1.5 km AGL within the upper portion of the BL, which is shallower earlier on and deepens gradually due to surface heating (Figs. 6a–c). The parcel descends slightly between 2050 and 2100 UTC (Fig. 6a) before starting a slow ascent until 2127 UTC (Figs. 6a–c), accompanying the evolution of gentle downdrafts and updrafts in a shallower BL. During this period, the near-surface convergence forcing that the parcel follows is weak, and makes less of a contribution to lift the parcel. By 2130 UTC (Fig. 6d), the near-surface convergence forcing becomes

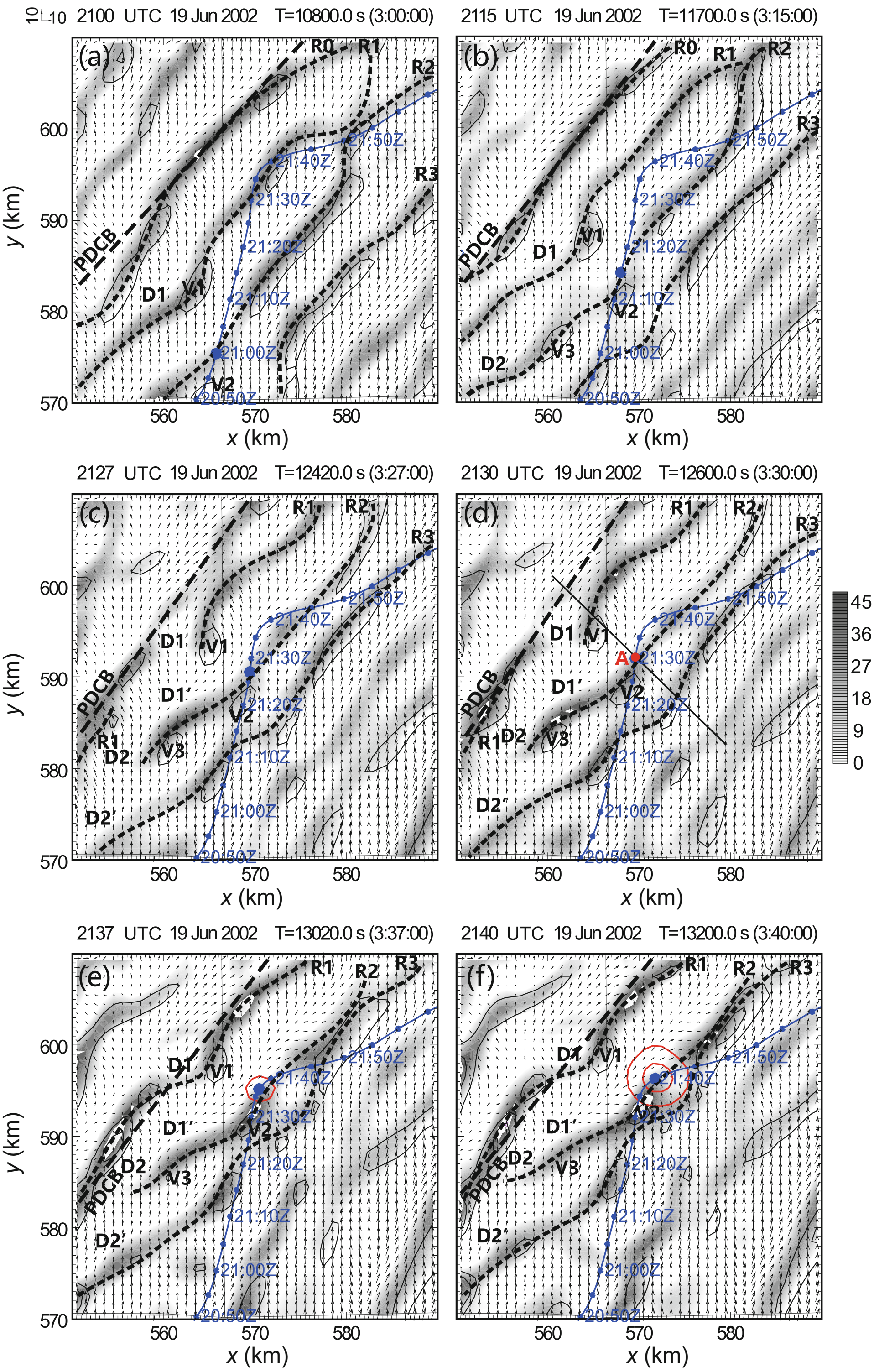

Fig. 5. Model-predicted near-surface (about 30 m AGL) moisture convergence field (gray shading; values amplified by a factor of 1000; only positive values shown), horizontal wind vectors (vector key shown in the plots; units: m s^{-1}), vertical vorticity field (black contours; only 100, 200 and 300×10^{-5} s^{-1} contours shown), and composite reflectivity (thick red contours; only 10, 20 and 30 dB*Z* contours plotted) for the CI at (a) 2100, (b) 2115, (c) 2127, (d) 2130, (e) 2137 and (f) 2140 UTC 19 June 2002. The domain corresponds to the boxed region in Fig. 3. A trajectory of a representative parcel feeding the first initiated cell (in blue) is overlaid, together with the times for the parcel locations along the trajectory, with the parcel location at the time of each plot shown in a large blue dot. The PDCB is shown as a long-dashed line; RCBs are shown by short-dashed lines labeled with “Rn” (where “n” is an integer number); and “Dn” and “Vn” indicate locations of divergence centers and mesocyclones. The thin straight line in (d) shows the position of a vertical cross section in Fig. 7; the red dot A in (d) denotes the sounding position in Fig. 8.

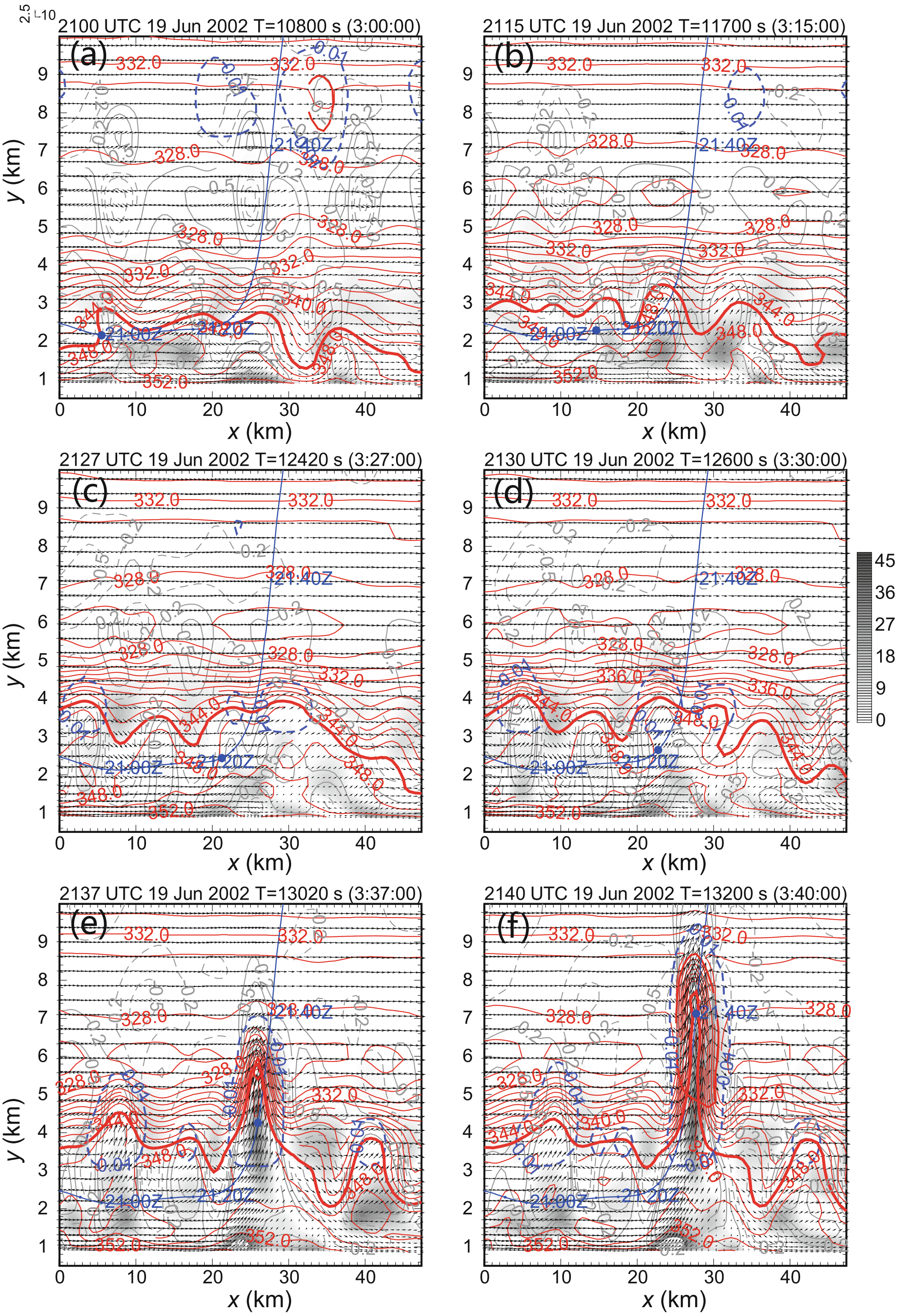

Fig. 6. Vertical cross sections along the parcel trajectory in Fig. 5 at (a) 2100, (b) 2115, (c) 2127, (d) 2130, (e) 2137 and (f) 2140 UTC 19 June 2002. Shown are the model-predicted moisture convergence field (gray shading; values amplified by a factor of 1000; only positive values shown), wind vectors (vector key shown in the plots; units: m s^{-1}), equivalent potential temperature (thin red contours; units: K), vertical velocity (thin gray contours; positive solid and negative dashed; units: m s^{-1}), and composite reflectivity of 10 dBZ (thick solid red contours). The cloud is outlined with 0.01 g kg^{-1} thick dashed blue contours of total condensed water and ice in the plots. The bold contour of θ_e at 346 K denotes the extent of the CBL. The blue dot along the blue trajectory indicates the location of the parcel on the trajectory at the time of each plotted panel.

stronger and begins to contribute more to the updraft, lifting the parcel with the vertical velocity of more than 1 m s^{-1}. The near-surface convergence forcing becomes even broader and stronger as R2 gets further enhanced below the parcel (Figs. 5e and f, Figs. 6e and f). It is clear that the upward forcing of the locally enhanced RCB helps to quickly raise the parcel to lead to the CI. In fact, the updraft quickly lifting the parcel involves upward forcing of the locally enhanced RCB together with the mesoscale PDCB convergence, which is discussed next.

3.3. *Combined upward forcing of the RCB and the mesoscale PDCB convergence*

Figure 7a shows a vertical cross section that is roughly perpendicular to the PDCB and the RCBs, and through the parcel shortly before the CI time at 2130 UTC. The mesoscale PDCB convergence exhibits an upward moisture bulge and a deeper BL, while the BL out of the bulge is shallower. Note that the vertical cross section along the parcel trajectory in Fig. 6 is not through the PDCB but roughly parallel to the PDCB (see Fig. 5); the extent of the BL along the cross section in Fig. 6 has less difference than that shown in Fig. 7.

The HCR circulations can be indicated by updraft and downdraft pairs within the BL in Fig. 7a, and are more clearly shown in perturbation wind vectors along the cross section in Fig. 7b. The parcel trajectory projected to this cross section suggests that the upward forcing of the HCR convergence or RCB within the shallower BL is not strong enough to lift the representative parcel above its level of free convection to initiate convection. Within the deeper BL, meanwhile, the updrafts associated with HCR circulations are stronger and extend higher due to the mesoscale PDCB convergence forcing, and have resulted in the formation of two clouds by 2130 UTC. It is unsurprising that the cloud above R2 initiates first as convection, since R2 gets much enhanced locally and the associated upward forcing evidently strengthens the updraft that lifts the representative parcel.

The deepening of the BL associated with the CI is a combined result of surface heating and the mesoscale PDCB convergence, and is illustrated using the evolution of model-extracted sounding near the CI location in Fig. 8. At 2030 UTC, there still exists a weak stable layer between 850 and 800 hPa with a CIN of 8 J kg^{-1}. By 2100 UTC, surface heating has eroded the cap. Between 600 and 400 hPa is a layer of air with near neutral stability and low moisture content; this layer of air is from west of the PDCB and is gradually lifted by the mesoscale PDCB convergence forcing. By 2130 UTC, the atmosphere is already neutrally stable below 650 hPa and the CAPE has accumulated up to 4024 J kg^{-1} from 3494 J kg^{-1} at 2030 UTC. The moisture is essentially constant between 800 and 650 hPa due to a well-mixed BL, while the gradual change of moisture below 800 hPa should be associated with the local enhancement of near-surface moisture convergence and its upward transfer. The evolution of the sounding is consistent with the discussion above that the combined upward forcing of the RCB and the mesoscale PDCB convergence lifts the representative air parcel above its level of free convection to initiate convection.

4. Summary and conclusion

In this paper, the 19 June 2002 CI case from the IHOP_2002 field experiment is further investigated using the output from a successful high-resolution numerical simulation. In particular, the CI that occurred in the IHOP_2002 region associated with a dryline is further analyzed by examining the interaction of BL HCRs with each other and with the dryline. The additional forcing associated with the evolu-

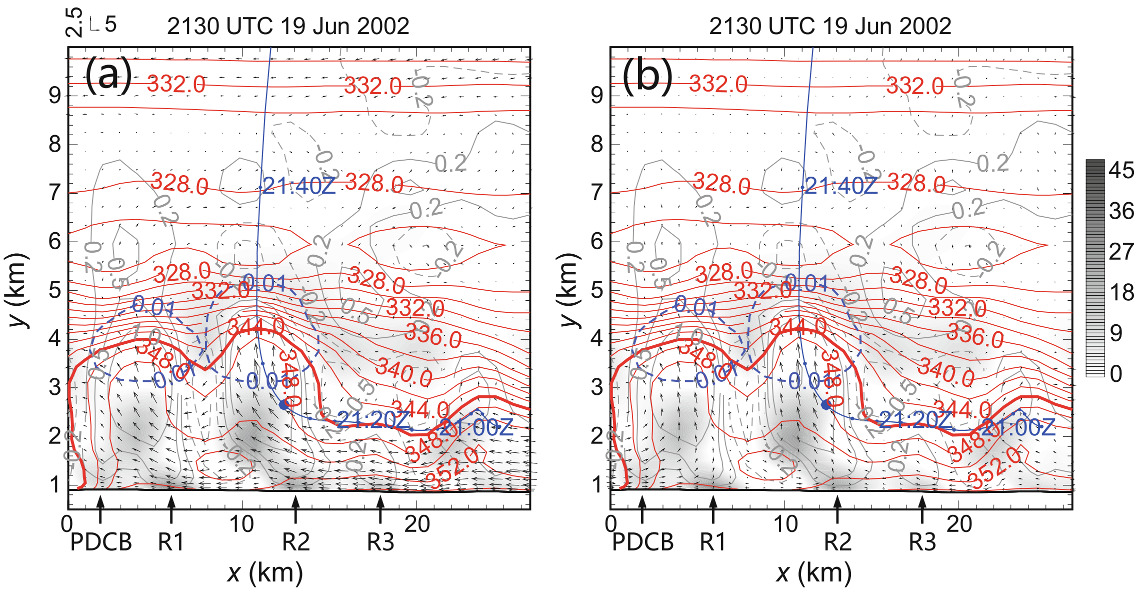

Fig. 7. The same fields plotted in Fig. 6, but for the cross section through the line in Fig. 5d. The plots of (b) are reproduced from (a) with the horizontal wind averaged at each level along the cross section subtracted at that level. The positions of the defined boundary and RCBs are denoted as upward pointed arrows.

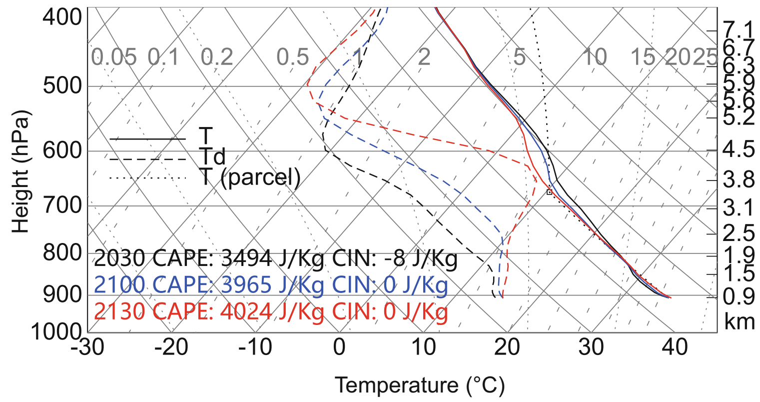

Fig. 8. Skew-T plots of soundings extracted from model forecasts at A in Fig. 5d, at 2030, 2100, and 2130 respectively.

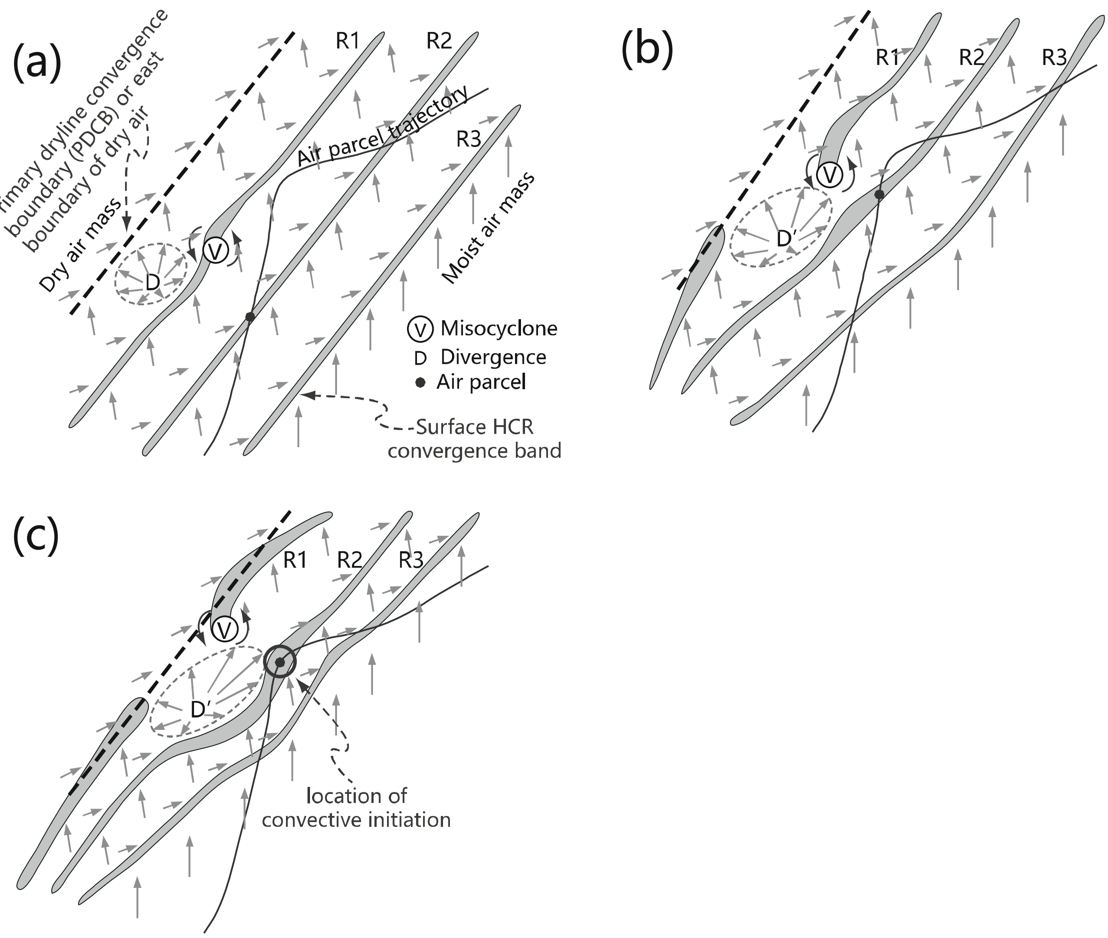

Fig. 9. Conceptual model of localized near-surface convergence forcing supporting the CI due to the interaction of the RCBs on the east side of the PDCB. The near-surface features (a) about 30 and (b) 10 min before the CI, and (c) at the CI time. The PDCB and RCBs are denoted as long-dashed line and shaded bands respectively. The labels “Rn” (where “n” is an integer number), “D”, “D′” and “V” indicate different RCBs, divergence centers and mesocyclones, respectively. The width of the shaded band indicates the strength of the convergence associated with the RCB. Representative winds are shown as arrows, with longer length meaning stronger wind speed. The thin curve denotes the trajectory of the parcel tracing the initiation of the cell, with the dot showing its position along the trajectory. The parcel stays about 1–1.5 km above ground before being evidently uplifted. See text for details.

tion of BL HCRs is carefully analyzed, which superimposes on the mesoscale forcing associated with the dryline and contributes to the initiation of localized convection.

On the east side of the dryline, prominent HCRs roughly parallel to the PDCB develop within the CBL due to surface heating, in the hours leading to CI. The role of the HCRs or

RCBs in the CI is analyzed by examining the effect of upward forcing of the RCBs on the representative air parcel forming the initial precipitating updraft of the convective cell. Backward trajectory analysis shows that the air parcel primarily originates at about 1–1.5 km above ground, and is within the upper portion of a shallower convective BL before moving into the deeper BL associated with the mesoscale PDCB convergence forcing.

The processes of RCB reorganization are summarized in a conceptual model in Fig. 9. On the moist side of the PDCB, the HCRs primarily parallel to the PDCB are driven by the south-to-southeast winds toward the PDCB as the CBL deepens with time. First, a mesocyclone, V, begins to develop along R1 due to nonuniform interaction of the PDCB with R1, accompanying the formation of a divergence center, D, between the PDCB and R1 to the southwest of V. The divergence center shows stronger north-to-northwest divergent flow due to downward transport of southerly momentum, and V will be strengthened when R1 is further distorted by D (Fig. 9a). Later, the circulation of V breaks R1 and the south portion of R1 quickly merges with the PDCB (Fig. 9b). Then, a new divergence center, D', quickly develops between the PDCB and R2 (Fig. 9b). The interaction of R2 with the quickly developed D' and the approaching R3 results in evident local enhancement of R2 (Fig. 9c). The local maximal convergence along the near-surface RCB will induce locally enhanced upward forcing to lift the representative air parcel that follows and stays on top of the RCB as the RCB moves toward the PDCB.

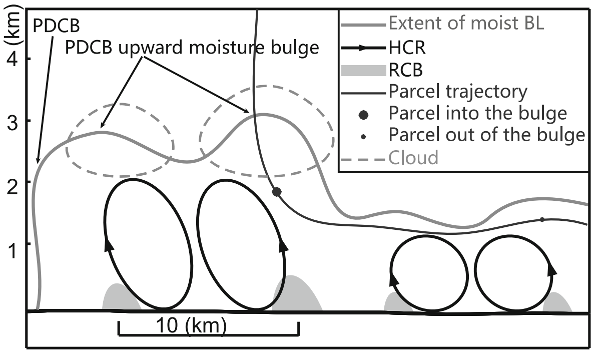

Fig. 10. Conceptual model of CI due to combined upward forcing of the RCB and the mesoscale PDCB convergence. The representative air parcel feeding the CI originates at about 1–1.5 km above ground within the upper portion of the moist BL. Earlier on, the BL is shallower, and the RCB upward forcing that the parcel follows is not enough to initiate convection. As the RCBs spaced roughly 10 km apart get close to and interact with the PDCB, they reorganize and form locally enhanced near-surface convergence forcing below the parcel, as depicted in Fig. 9. The BL associated with the PDCB upward moisture bulge is deeper than that out of the bulge. The HCRs within the bulge extend higher and are stronger due to the mesoscale PDCB convergence forcing. The combined upward forcing of the locally enhanced near-surface convergence forcing and the extended HCR with stronger updraft within the bulge quickly lifts the representative air parcel above its level of free convection to first initiate convection. Note the parcel is from the south side of the cross section, and the trajectory shown is a projection of its true trajectory to this cross section.

In fact, it is the combined upward forcing of the locally enhanced RCB and the mesoscale PDCB convergence that makes the CI occur first at the particular point on the RCB. When the BL is shallower earlier on, the upward forcing of the RCB that the parcel follows is not enough to initiate convection. As the RCBs get close to and interact with the PDCB, they reorganize and induce locally enhanced near-surface convergence forcing below the parcel, as illustrated in Fig. 9. The deeper BL exhibits a moisture bulge and extended HCRs with stronger updrafts due to the mesoscale PDCB convergence forcing. As the parcel enters into the deeper BL, the combined upward forcing of the locally enhanced near-surface convergence forcing and the mesoscale PDCB convergence forcing quickly lifts the representative air parcel above its level of free convection to initiate convection. A conceptual model of the CI is summarized in Fig. 10.

Acknowledgements. This work was supported by the National Key R&D Program of China (Grant No. 2017YFC1501603), the China National Program on Key Basic Research Project (973 Program) (Grant No. 2013CB430103), and the National Natural Science Foundation of China (Grants Nos. 41775054, 41375061 and 40705019). Assistance was provided by Dr. Keith BREWSTER when preparing some initial data. Appreciation is also extended to Yunheng WANG, Fanyou KONG, Jidong GAO and Guoqing GE for their help with ARPS/ARPS3DVAR. The NCEP Eta Model analyses used to initialize the simulation were downloaded from the NCAR Data Archive. A Sun Constellation Linux cluster, Ranger, operated by TACC of the University of Texas, and a Linux cluster operated by OSCER of the University of Oklahoma, were used for the computations.

REFERENCES

Atkins, N. T., R. M. Wakimoto, and C. L. Ziegler, 1998: Observations of the finescale structure of a dryline during VORTEX 95. *Mon. Wea. Rev.*, **126**, 525–550, https://doi.org/10.1175/1520-0493(1998)126<0525:OOTFSO>2.0.CO;2.

Bluestein, H. B., and S. S. Parker, 1993: Modes of isolated, severe convective storm formation along the dryline. *Mon. Wea. Rev.*, **121**, 1354–1372, https://doi.org/10.1175/1520-0493(1993)121<1354:MOISCS>2.0.CO;2.

Browning, K. A., and Coauthors, 2007: The convective storm initiation project. *Bull. Amer. Meteor. Soc.*, **88**, 1939–1956, https://doi.org/10.1175/BAMS-88-12-1939.

Fritsch, J. M., and R. E. Carbone, 2004: Improving quantitative precipitation forecasts in the warm season: A USWRP research and development strategy. *Bull. Amer. Meteor. Soc.*, **85**, 955–965, https://doi.org/10.1175/BAMS-85-7-955.

Gao, J. D., M. Xue, K. Brewster, and K. K. Droegemeier, 2004: A three-dimensional variational data analysis method with recursive filter for Doppler radars. *J. Atmos. Oceanic Technol.*, **21**, 457–469, https://doi.org/10.1175/1520-0426(2004)021<0457:ATVDAM>2.0.CO;2.

Hane, C. E., C. L. Ziegler, and H. B. Bluestein, 1993: Investigation of the dryline and convective storms initiated along the dryline: Field experiments during COPS-91. *Bull. Amer. Meteor. Soc.*, **74**, 2133–2145, https://doi.org/10.1175/1520-0477(1993)074<2133:IOTDAC>2.0.CO;2.

Hane, C. E., R. M. Rabin, T. M. Crawford, H. B. Bluestein, and M. E. Baldwin, 2002: A case study of severe storm development along a dryline within a synoptically active environment. Part II: Multiple boundaries and convective initiation. *Mon. Weat. Rev.*, **130**, 900–920, https://doi.org/10.1175/1520-0493(2002)130<0900:ACSOSS>2.0.CO;2.

Liu, H. X., and M. Xue, 2008: Prediction of convective initiation and storm evolution on 12 June 2002 during IHOP_2002. Part I: Control simulation and sensitivity experiments. *Mon. Wea. Rev.*, **136**, 2261–2282, https://doi.org/10.1175/2007MWR2161.1.

Murphey, H. V., R. M. Wakimoto, C. Flamant, and D. E. Kingsmill, 2006: Dryline on 19 June 2002 during IHOP. Part I: Airborne doppler and LEANDRE II analyses of the thin line structure and convection initiation. *Mon. Wea. Rev.*, **134**, 406–430, https://doi.org/10.1175/MWR3063.1.

Peckham, S. E., R. B. Wilhelmson, L. J. Wicker, and C. L. Ziegler, 2004: Numerical simulation of the interaction between the dryline and horizontal convective rolls. *Mon. Wea. Rev.*, **132**, 1792–1812, https://doi.org/10.1175/1520-0493(2004)132<1792:NSOTIB>2.0.CO;2.

Richard, E., A. Buzzi, and G. Zängl, 2007: Quantitative precipitation forecasting in the Alps: The advances achieved by the Mesoscale Alpine Programme. *Quart. J. Roy. Meteor. Soc.*, **133**, 831–846, https://doi.org/10.1002/qj.65.

Shaw, B. L., R. A. Pielke, and C. L. Ziegler, 1997: A three-dimensional numerical simulation of a great plains dryline. *Mon. Wea. Rev.*, **125**, 1489–1506, https://doi.org/10.1175/1520-0493(1997)125<1489:ATDNSO>2.0.CO;2.

Trier, S. B., G. S. Romine, D. A. Ahijevych, R. J. Trapp, R. S. Schumacher, M. C. Coniglio, and D. J. Stensrud, 2015: Mesoscale thermodynamic influences on convection initiation near a surface dryline in a convection-permitting ensemble. *Mon. Wea. Rev.*, **143**, 3726–3753, https://doi.org/10.1175/MWR-D-15-0133.1.

Wang, Q.-W., and M. Xue, 2012: Convective initiation on 19 June 2002 during IHOP: High-resolution simulations and analysis of the mesoscale structures and convection initiation. *J. Geophys. Res.*, **117**, D12107, https://doi.org/10.1029/2012JD017552.

Weckwerth, T. M., and D. B. Parsons, 2006: A review of convection initiation and motivation for IHOP_2002. *Mon. Wea. Rev.*, **134**, 5–22, https://doi.org/10.1175/MWR3067.1.

Weckwerth, T. M., and Coauthors, 2004: An overview of the international H_2O project (IHOP_2002) and some preliminary highlights. *Bull. Amer. Meteor. Soc.*, **85**, 253–278, https://doi.org/10.1175/BAMS-85-2-253.

Wilson, J. W., and R. D. Roberts, 2006: Summary of convective storm initiation and evolution during IHOP: Observational and modeling perspective. *Mon. Wea. Rev.*, **134**, 23–47, https://doi.org/10.1175/MWR3069.1.

Wulfmeyer, V., and Coauthors, 2008: RESEARCH CAMPAIGN: The convective and orographically induced precipitation study. *Bull. Amer. Meteor. Soc.*, **89**, 1477–1486, https://doi.org/10.1175/2008BAMS2367.1.

Xue, M., and W. J. Martin, 2006a: A high-resolution modeling study of the 24 May 2002 dryline case during IHOP. Part I: Numerical simulation and general evolution of the dryline and convection. *Mon. Wea. Rev.*, **134**, 149–171, https://doi.org/10.1175/MWR3071.1.

Xue, M., and W. J. Martin, 2006b: A high-resolution modeling study of the 24 May 2002 dryline case during IHOP. Part II: Horizontal convective rolls and convective initiation. *Mon. Wea. Rev.*, **134**, 172–191, https://doi.org/10.1175/MWR3072.1.

Xue, M., K. K. Droegemeier, and V. Wong, 2000: The Advanced Regional Prediction System (ARPS)—A multi-scale nonhydrostatic atmospheric simulation and prediction model. Part I: Model dynamics and verification. *Meteor. Atmos. Phys.*, **75**, 161–193, https://doi.org/10.1007/s007030070003.

Xue, M., and Coauthors, 2001: The Advanced Regional Prediction System (ARPS)—A multi-scale nonhydrostatic atmospheric simulation and prediction tool. Part II: Model physics and applications. *Meteor. Atmos. Phys.*, **76**, 143–165, https://doi.org/10.1007/s007030170027.

Ziegler, C. L., and C. E. Hane, 1993: An observational study of the dryline. *Mon. Wea. Rev.*, **121**, 1134–1151, https://doi.org/10.1175/1520-0493(1993)121<1134:AOSOTD>2.0.CO;2.

Ziegler, C. L., and E. N. Rasmussen, 1998: The initiation of moist convection at the dryline: Forecasting issues from a case study perspective. *Wea. Forecasting*, **13**, 1106–1131, https://doi.org/ 10.1175/ 1520-0434(1998)013<1106:TIOMCA>2.0.CO;2.

Ziegler, C. L., W. J. Martin, R. A. Pielke, and R. L. Walko, 1995: A modeling study of the dryline. *J. Atmos. Sci.*, **52**, 263–285, https://doi.org/10.1175/1520-0469(1995)052<0263:AMSOTD>2.0.CO;2.